

n-Heptane under Pressure: Structure and Dynamics from Molecular Simulations

M. Krishnan[†] and Sundaram Balasubramanian*

Chemistry and Physics of Materials Unit, Jawaharlal Nehru Centre for Advanced Scientific Research, Jakkur, Bangalore 560 064, India

Received: July 14, 2004; In Final Form: August 16, 2004

Atomistic molecular dynamics simulations have been performed in the isothermal–isobaric ensemble to explore the phase behavior of *n*-heptane. Motivated by recent high-pressure spectroscopic experiments on *n*-heptane, the present work aims at understanding the liquid–solid and the alluded to solid–solid transitions upon increasing pressure. Starting from the stabilized solid phase at 300 K and 10 kbar, we have investigated the range of these two transitions by a gradual decrease and increase of pressure, respectively. Although the solid–liquid transition has clear signatures such as the formation of gauche defects along the molecular backbone, the present model does not show any sign of a first-order solid–solid transition at high pressures. However, interesting changes in the environment around methyl groups and in their dynamics are observed. These have been substantiated by calculations of the vibrational density of states obtained from a normal-mode analysis and from the simulation trajectory.

1. Introduction

A common element of several complex molecular systems is the presence of an alkyl group.¹ It forms a crucial component of a wide variety of systems ranging from membranes, micelles, self-assembled monolayers,² and even molten salts.³ Thus, a study of the phase diagram of linear and branched alkanes continues to be interesting and relevant to the understanding of complex phenomena. Alkanes are also important in their own right; the long-chain ones are active components of lubricants, and short-chain alkanes such as *n*-heptane are employed as solvents. Mixtures of liquid *n*-heptane with isooctane are also used as standards to characterize the anti-knocking properties of engine fuel.⁴ Crystalline linear alkanes also exhibit interesting rotator phases that have been well studied through neutron-scattering experiments⁵ and computer simulations.⁶ The structure and dynamics of crystalline *n*-alkanes has been the subject of renewed interest lately.^{7–9}

In a recent study of the vibrational spectra of *n*-heptane under high pressure, Chronister and co-workers reported the occurrence of a possible solid–solid phase transition near 30 kbar.¹⁰ The experiments, performed at room temperature, also investigated the liquid–solid transition that takes place at around 12–15 kbar. The presence of a large number of gauche defects in the liquid state produces large broadening of the infrared peaks, in contrast to sharp bands in the crystal. However, the nature of the solid–solid transition was not clear from this study. Near 30 kbar in the solid state, they observed (i) a split in the asymmetric CH₃ and CH₂ bending modes in the 1400–1500-cm^{−1} region and (ii) a change in the slope of the line width as a function of pressure for the C–C stretching modes and the antisymmetric CH₃ mode. Specifically, the underlying structural changes (if any) that cause these splitting of the peaks and changes in their line widths are yet to be studied. In view of this, we have undertaken a comprehensive investigation of *n*-heptane under pressure using computer simulation methods. We report molecular dynamics (MD)

calculations of *n*-heptane performed at a temperature of 300 K and at pressures ranging from 1 to 70 kbar. Our goals are (i) to find out whether these transitions can be observed in computer models and (ii) to study the structural and dynamical behavior of the system as a function of pressure. In anticipation of our results, we observe signatures of the liquid–solid transition. At higher pressures in the crystalline state we do not find any clear evidence for a solid–solid-phase transition. However, we observe a dynamical arrest of the rotation of the methyl end groups and shifts in the vibrational features at such high pressures. Our simulations also point to extensive changes in the environment around the end groups of the alkane as a function of pressure.

2. Simulation Details

n-Heptane crystallizes in a triclinic cell (space group $P\bar{1}$) with the following lattice parameters:¹¹ $a = 4.15$ Å, $b = 19.97$ Å, $c = 4.69$ Å, $\alpha = 91.3^\circ$, $\beta = 74.3^\circ$, and $\gamma = 85.1^\circ$. The crystal density is 0.890 gm/cm³. The unit cell consists of two molecules that adopt the all-trans conformation. The chain axis of each molecule makes an angle of 2° with the ab plane and 71° with the a axis. This experimental crystal structure was generated and used as the initial configuration for our molecular dynamics calculations. The simulation box consisted of a total of 128 such unit cells: 8 unit cells each along the \bar{a} and \bar{c} axes and 2 along the \bar{b} axis. We have used an all-atom representation for the description of *n*-heptane.¹³ This model has previously been used to characterize the phase behavior of *n*-octane in the bulk¹⁴ and the organization of *n*-hexane on graphite.¹⁵ Although such a model increases the computational cost, it is inevitable in studies of molecular crystals, particularly at high pressures, where steric effects are expected to play a significant role.¹² Thus, the simulated crystal consisted of 256 molecules with a total of 5888 atoms. The interaction potential contained bond stretching and bending and torsional and nonbonded interactions of the Williams type. Its form and the parameters are the same as reported in ref 13. To mimic the high-pressure experiments closely,¹⁰ we have carried out the simulations in the constant temperature and constant pressure (NPT) ensemble. Pressure

* Corresponding author. E-mail: bala@jncasr.ac.in.

[†] E-mail: mkrishna@jncasr.ac.in.

control was achieved through the Parrinello–Rahman algorithm^{16,17} that allows the simulation cell to vary both its shape and size. A Nosé–Hoover chain thermostat¹⁸ attached to the system controlled the temperature. The molecular model was considered to be fully flexible, and interaction potentials for the bond stretches, bends, and torsional angles were applied. The equations of motion were integrated using the reversible reference system propagator algorithm (RESPA)¹⁹ with an outer time step of 4 fs. The innermost time step that handled the C–H vibrations was 0.5 fs. Long-range interactions were thus integrated with the full time step of 4 fs, whereas the short-range forces were integrated with a time step of 2 fs. The torsional degrees of freedom were solved for a time step of 1 fs, and bond bending and stretching interactions were handled for a time resolution of 0.5 fs. The potential of interaction was cut off at 12 Å, and long-range corrections to energy and pressure were calculated using standard methods.²⁰ The calculations were carried out using the molecular dynamics package PINY_MD on a parallel computer.²¹

The initial configuration for the MD runs was based on the experimental structure at 100 K. To check the veracity of the empirical interaction potentials used in this study, we first performed molecular dynamics simulations in the canonical ensemble at a temperature of 100 K and a pressure of 1 bar. The system was equilibrated for 450 ps, followed by a production run of 400 ps during which time the lattice parameters of the simulated crystal were monitored as a function of time. We found the system to be stable with average lattice parameters as follows: $a = 4.15$ Å, $b = 20.01$ Å, $c = 4.51$ Å, $\alpha = 91.2^\circ$, $\beta = 76.25^\circ$, and $\gamma = 86.56^\circ$, in good agreement with X-ray diffraction data. The maximum difference in the cell parameters between simulations and experiment is 4%, and the density is predicted to within 2%. The equilibrated system obtained from the above run was used as a starting configuration for the constant-pressure simulations. Note that the spectroscopy studies of Chronister et al. on *n*-heptane were performed at 300 K, where *n*-heptane is in the liquid phase at atmospheric pressure. Upon a gradual increase in pressure, they report two transitions: the liquid–solid transition at around 14 kbar and a solid–solid transition near 30 kbar. The simulation pathway follows a different protocol than that of the experiment; one cannot start the simulation from a liquid state at 1 bar of pressure (at 300 K) and increase the pressure because the process of crystallization is time-consuming, beyond the limits of atomistic computer simulations. However, direct heating of the crystal that was equilibrated at 100 K and 1 bar to 300 K would melt it or at least induce considerable disorder, and an ordered lattice that is expected at higher pressures will be impossible to attain. To overcome this limitation in the computational procedure, we have employed a procedure that is different from the experiment. We stabilized the solid phase at 300 K and 10 kbar by tracing a path in the phase diagram of *n*-heptane that starts with the crystal at 100 K and 1 bar. Stepwise heating followed by a gradual application of pressure was then carried out. Specifically, we heated the crystal in steps of 50 K starting from 100 K up to 300 K. At each temperature, the system was equilibrated for 400 ps, followed by an increase in pressure of 5 kbar with a corresponding equilibration run of 300-ps duration. We followed this procedure up to 300 K and 10 kbar, where we found the solid phase to be stable. Maintaining the temperature at 300 K, we could study both the reported solid–solid transition by increasing the pressure or the liquid–solid transition by decreasing the applied pressure. At 300 K, the system was studied at pressures ranging from 10 kbar to

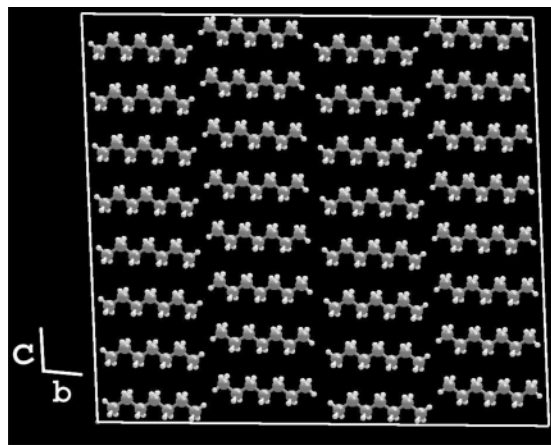


Figure 1. Crystal structure of *n*-heptane as used in our simulations shown as a view through the \vec{a} axis. The gray spheres represent carbon atoms, and the white spheres denote hydrogen atoms.

70 kbar in steps of 2.5 kbar. At each pressure, MD runs were performed for 100 ps. Additional runs of 2-ns duration were carried out at selected nine pressures for analyses.

The vibrational density of states (VDOS) was calculated by two methods. A normal-mode analysis by analyzing the eigenvalue spectrum of the Hessian matrix yielded the VDOS within the harmonic approximation. The exact, classical VDOS was also computed as the power spectrum of the velocity autocorrelation function of the atoms. For the latter, 20-ps long trajectories in which atomic velocities were stored every time step were generated at each pressure. The power spectrum was obtained as an average from five such independent trajectories that were each separated by 20 ps. The spectra were convoluted with a Gaussian function of spread 4 cm^{-1} so as to mimic a line shape. Details of the normal-mode analysis (NMA) and its application to the vibrational spectrum of poly(ethylene oxide) have been provided.²²

3. Results and Discussion

In the following discussion, results at high pressure are compared to those obtained from the crystal at 10 kbar and 300 K.

3.1. Crystal Structure, Volume, and Energetics. *n*-Heptane crystallizes in a triclinic unit cell with $Z = 2$.¹¹ Figure 1 shows the molecular arrangement in the crystal. The molecules are arranged in layers. Within each layer, a given molecule is surrounded by six neighbors. The application of pressure in the crystalline phase leads to interesting and subtle changes in the environment of the terminal methyl groups.

We have examined the variation of cell lengths as a function of pressure. These were averaged over configurations obtained from the molecular trajectory of duration 400 ps. Their monotonic decrease (Figure 2a) with increasing pressure suggests the absence of a first-order phase transition in the solid phase. The relative changes in the cell lengths with respect to the values at 10 kbar (Figure 2a) reveal a greater effect on the a and c axes compared to that on the b axis. Note that the molecular axis is nearly oriented along the b axis of the crystal. Thus, the difference in pressure dependence indicates that the molecular packing along the b axis is different from that along the a and c axes. The smaller relative change in the b parameter with increasing pressure suggests that the crystal is densely packed along the b axis as compared to the packing in the other two directions. As a consequence of this distinction, nearest-neighbor methyl–methyl distances are shorter along the b axis

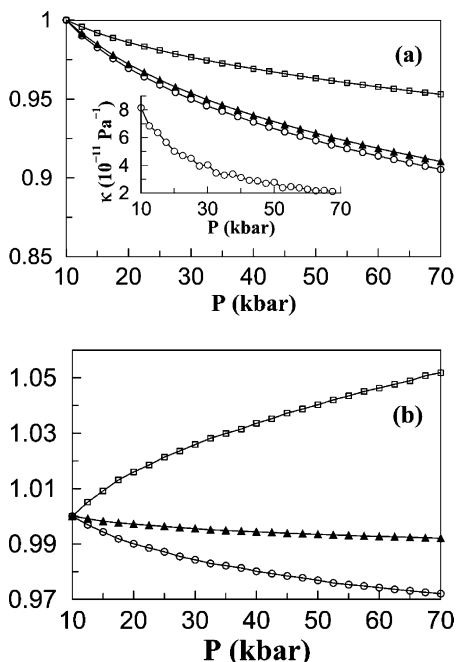


Figure 2. Pressure dependence of (a) cell lengths (a, \square ; b, \square ; and c, \blacktriangle) and (b) cell angles (α , \blacktriangle ; β , \square ; and γ , \circ). The values are normalized with respect to their magnitude at 10 kbar. The inset to graph (a) shows the isothermal compressibility as a function of pressure.

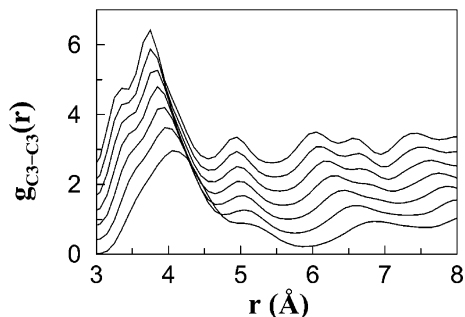


Figure 3. Radial distribution function $g_{\text{C3-C3}}(r)$ shown at various pressures. The functions are shifted for clarity. Pressures (from bottom to top): starting from 10 up to 70 kbar in steps of 10 kbar.

than along the a and c axes. (See the discussion of Figure 4 later.) By examining the variation of the unit cell volume with pressure, we have calculated the isothermal compressibility, which is defined as²³

$$\kappa = -\frac{1}{V} \left(\frac{dV}{dP} \right)_T \quad (1)$$

where V is volume, P is pressure, and T is temperature. The pressure dependence of the isothermal compressibility (κ) is shown in the inset of Figure 2a, which also exhibits only a monotonic decay with no discontinuities. Similarly, an examination of the variation of the cell angles with pressure reveals a larger relative change in the β parameter (Figure 2b) than in the other two angles, indicating a larger change in intermolecular structure. The variation of the density of the n -heptane crystal with pressure calculated from this study is given in Table 1 for a few selected pressures. The density increases monotonically with pressure. The internal energy of the system (not shown) increases with pressure without any discontinuities.

3.2. Structure around Terminal Group. **3.2.1. Pair Correlation Functions.** The changes in the intermolecular structure exhibit a pattern that is consistent with our observations of the

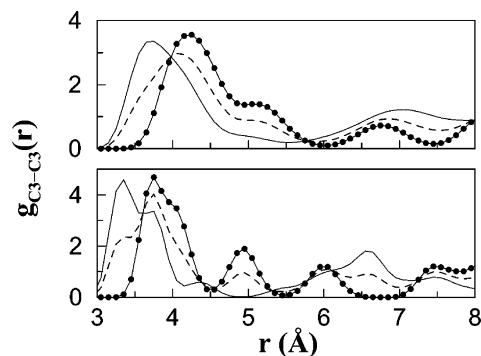


Figure 4. C3–C3 radial distribution functions to show the contribution from intra- and interlayer neighbors. Solid line: $g_{\text{interlayer}}(r)$; Solid line with filled circles: $g_{\text{intralayer}}(r)$; Dashed line: full $g(r)$; top panel: at 10 kbar; bottom panel: at 70 kbar.

TABLE 1: Density, ρ , of n -Heptane at Selected Pressures, P , from Simulation

P (kbar)	ρ (gm/cm ³)
10	0.98
20	1.05
30	1.10
40	1.14
50	1.17
60	1.20
70	1.23

cell parameters above. In Figure 3, we show the intermolecular pair correlation functions, $g(r)$, of CH₃–CH₃ pairs. For simplicity, the carbon atom of the methyl group will henceforth be denoted as C3, that of the methylene group, as C2, and the hydrogens of the methyl groups, as H3. With increasing pressure, two distinct features in the C3–C3 $g(r)$ are discernible. The first peak develops a shoulder at around 3.3 Å, and the broad hump present near 5.2 Å at 10 kbar grows into a formal peak. The coordination number, integrated up to the minimum of the first peak (5.9 Å at 10 kbar and 5.45 Å at 70 kbar), is around 10.3, whereas the corresponding value at the start of the hump (4.9 Å at 10 kbar and 4.55 Å at 70 kbar) is 8. The main peak present at around 4 Å at 10 kbar shifts to smaller distances with increasing pressure, as expected.

To gain a better understanding of the nearest-neighbor structure of a methyl carbon, we have subdivided the C3–C3 $g(r)$ into intra- and interlayer contributions. $g_{\text{intralayer}}(r)$ is the pair correlation function of a central C3 with other methyl carbons that are in the same layer as itself, and $g_{\text{interlayer}}(r)$ is the pair correlation function of C3 with methyl carbons that belong to adjacent layers. We show the behavior of these functions at 10 and 70 kbar in Figure 4. At low pressure (10 kbar), the $g_{\text{intralayer}}(r)$ function shows a broad peak at 4.25 Å, followed by a shoulder at 5.15 Å. We observe that four neighbors contribute to the peak at 4.25 Å whereas the next two neighbors give rise to the shoulder at 5.15 Å. At high pressure (70 kbar), these peak positions shift to lower r values, and the shoulder observed at 10 kbar emerges as a formal peak at 4.95 Å, indicating that the second coordination shell acquires a well-defined structure at high pressures. The coordination number up to the second shell does not change at high pressures. At 10 kbar, the $g_{\text{interlayer}}(r)$ function shown in Figure 4 exhibits a broad peak at 3.75 Å, whereas its tail stretches up to 5.5 Å. The coordination number calculated up to 5.5 Å is 4. At 70 kbar, we observe the $g_{\text{interlayer}}(r)$ to show subpeaks within the range of the first coordination shell (up to 4.9 Å), preserving the coordination number of 4. The formation of such subpeaks, keeping the coordination number intact, can be attributed to the

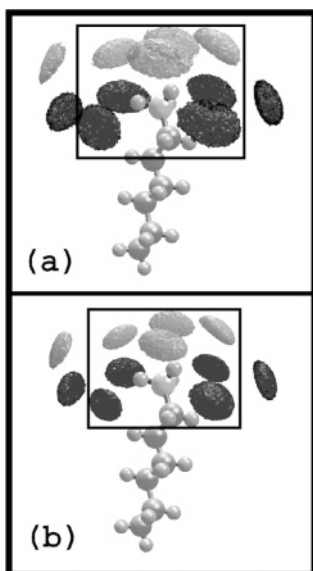


Figure 5. Atomic probability density map of a methyl carbon around a given methyl group shown up to its second coordination shell at (a) 10 (b) 70 kbar. The black lobes denote the probability density of finding neighboring methyl carbons that belong to same layer as the central methyl (grey sphere of the molecule shown), and the gray lobes denote that of adjacent-layer methyl carbons. The rectangular box is the boundary around the closest eight neighbors. Only the probability density values greater than 0.00008 methyl carbons/Å³ are shown.

structural rearrangement of the interlayer methyl carbons that lie within the first coordination shell of the central C3 atom. The contribution of the second peak ($r > 4.9$ Å) of the $g_{\text{interlayer}}(r)$ to the coordination number of the second peak of the total C3—C3 $g(r)$ (Figure 3) is 0.3. The above analysis leads to a clear picture of the environment around a methyl carbon atom at these two pressures and can be summarized as follows. The first subshell around the central C3 consists of eight methyl carbons: four are present in the same layer as the central C3, and the other four are present in the adjacent layers. The second subshell consists of 2.3 neighbors on average, of which more than 70 contributions come from molecules in the same layer (intralayer) and the rest come from adjacent layers. The arrangement of these neighbors at 10 and 70 kbar is shown in Figure 5 as a probability density map. It shows the locations of C3 atoms in the first and second coordination shells using different color schemes. Note the clear emergence of the 11th neighbor at 70 kbar in the top left corner. This density is only weakly present at 10 kbar. The pressure dependence of the radial distribution functions suggests the coordination shell around a C3 unit to be intact in quantity, although subtle differences in the location of the neighbors arise with increasing pressure. In addition, we find that the increase in pressure brings the molecules in the adjacent layer closer to a central methyl group.

In Figure 6a–c, we show the intermolecular pair correlation functions, $g(r)$, of C3—C2, C3—H3, and H3—H3 pairs, respectively. In contrast to the results for C3—C3 $g(r)$, the behavior of the C3—C2 $g(r)$ does not show any significant change with pressure.

Note the emergence of the hump around 3.5 Å in the C3—H3 radial distribution function shown in Figure 6b. The function at 70 kbar exhibits minima at 3.35, 4.05, and 5.3 Å. The running coordination numbers at these positions are 8.2, 15.7, and 31.0, respectively. The total coordination number of 31 hydrogens, when considered along with the 10 C3 atoms in the first coordination shell (as discussed in Figure 3), makes it tempting to conclude that each neighboring C3 provides the same number

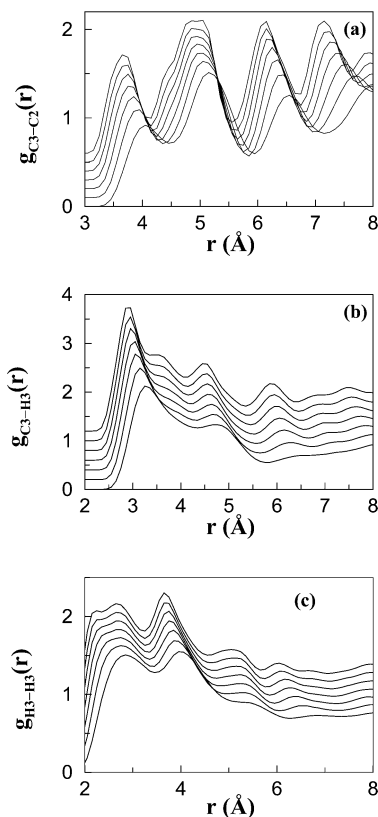


Figure 6. Radial distribution functions (a) $g_{\text{C3-C2}}(r)$, (b) $g_{\text{C3-H3}}(r)$, and (c) $g_{\text{H3-H3}}(r)$ shown at various pressures. The functions are shifted for clarity. Pressures (from bottom to top): starting from 10 up to 70 kbar in steps of 10 kbar.

of hydrogens (i.e., 3) to a central C3 group. However, this is not borne out by even a cursory visualization of a few molecules with their neighbors. The values of the C3—H3 $g(r)$ at these minima are too large. The only explanation consistent with this large magnitude is that each of the neighboring C3 groups contributes an unequal number of hydrogen atoms to the features present under the first peak of the C3—H3 $g(r)$. The H3—H3 $g(r)$ is shown in Figure 6c. Here too we see that the first peak is split at high pressure. It is rather difficult to attribute the origin of these peaks to (i) the presence of a large number of hydrogens or (ii) the rotation of the methyl groups. The latter is the reason for the rather large value of $g(r)$ at the minima.

3.2.2. Three-Body Correlation Functions. We delve into the environment around C3 by studying the angle distributions. In Figure 7a, we show the C3—C3—C3 angle distributions at various pressures. The triplets are chosen such that the atoms at the two ends of the triangle are within the first coordination shell of the central C3 atom. The distribution exhibits a large peak at an angle of 180°, which arises from neighboring pairs that are diagonally opposite to each other with respect to the central C3 atom. These pairs are performed in the same layer as the central atom. Systematic variations are observed at specific angles with increasing pressure. To identify the source of each of these peaks, we have divided the neighbors into two categories: those belonging to the same layer as the central C3 atom are called intralayer, and those that are present in the adjacent layer are called interlayer. The C3—C3—C3 angle distribution was again calculated at 70 kbar for triplets that are in the same layer and for those in which at least one C3 neighbor belonged to the adjacent layer. These distributions are shown in Figure 7b and c. We notice that the peaks at $\cos \theta$ values of -0.22 and $+0.22$ that are present in the full distribution (Figure

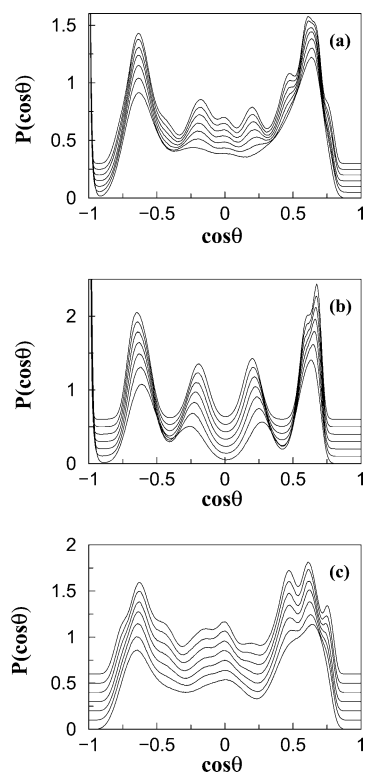


Figure 7. (a) Distribution of the cosine of the angle, θ , between the vectors that connect the central methyl carbon with any of the neighboring methyl carbons that lie within the second subshell of the central methyl group. The functions are shifted for clarity. Pressures (from bottom to top): starting from 10 up to 70 kbar in steps of 10 kbar. (b) Same as for part (a), with contributions from intralayer neighbors only. (c) Same as for part (a), with contributions from interlayer neighbors only.

7a) are present in the intralayer function but are absent in that for the interlayer. Thus, these features arise from neighbors that are present in the same layer as the central carbon atom. The angles corresponding to these values are around 102° and 80° respectively. These values are consistent with the probability density map of nearest neighbors discussed in Figure 5 and suggest a rhombuslike arrangement (upon projection onto a plane perpendicular to the chain axis) of intralayer neighbors around the central C3 atom. A similar analysis of the functions in Figure 7b and c shows that the peaks at $\cos \theta$ values of 0, 0.5, and 0.75 come purely from interlayer contributions. We also find that both intralayer and interlayer neighbors contribute to the large peaks at 0.3 and -0.68 . The peaks at 0.6 and 0.7 are due to the molecules in the intralayer that are coordinated as the 9th and 10th neighbors to the central C3 group. It is also pertinent to study the location of nearest-neighbor C3 atoms with respect to the C2–C3 bond (i.e., the methylene–methyl bond). In Figure 8, we show the angle distribution of C2–C3–C3 triplets at various pressures. All of the features that exist at 10 kbar increase in intensity with increasing pressure. However, a new peak emerges at a $\cos \theta$ value of -0.9 that can be ascribed to interlayer contributions through a similar analysis to that above. Note also the strong peak at a value of -1 that can arise again only out of interlayer C3 neighbors.

Do these increasing structural correlations observed in the C3–C3 pair correlation function, for instance, arise merely because of an increase in the density of the system? To answer this question, we have calculated the pair correlation function of one configuration of atoms that was obtained from the MD simulation at 10 kbar but whose atomic coordinates are scaled with the density of the simulated system at 70 kbar. The

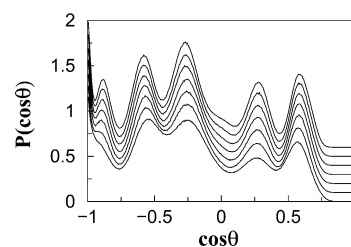


Figure 8. Distribution of the cosine of the angle, θ , between the terminal C2–C3 vector of the central molecule and the vector that connects the central methyl carbon with any of neighboring methyl carbons that lie within the second subshell of the central methyl group. Pressures (from bottom to top): starting from 10 up to 70 kbar in steps of 10 kbar.

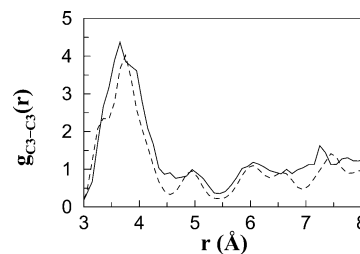


Figure 9. Reconstructed radial distribution function, $g_{\text{C3-C3}}(r)$ (—) (see text for definition), compared with that obtained from the actual MD trajectory at 70 kbar (---).

calculation proceeded as follows. Scaled atomic coordinates at 10 kbar were obtained as the product of the inverse of the simulation box matrix of 10 kbar and the real world coordinates. These scaled coordinates were converted to real units by unscaling them with the box matrix of 70 kbar. This procedure yields atomic coordinates that correspond to the low-pressure configuration and the high-pressure density. A variant of this method was used by Bagchi et al. to analyze the structure of liquid water at high pressure.²⁴ The “pseudo” or reconstructed $g(r)$ so obtained is compared to the true function at 70 kbar in Figure 9. The agreement between the true $g(r)$ at 70 kbar and that obtained from this procedure is striking. The shift in the first peak and the emergence of a large hump at 5 Å is captured quite well by this procedure. However, the small shoulder at 3.35 Å that is present at 70 kbar is absent in this reconstructed $g(r)$. However tempting it might be, one should not belittle the effort to obtain the true pair correlation functions at high pressure such as 70 kbar by actually carrying out the simulations. We draw the attention of the reader to Figure 2 (relative cell parameters versus pressure). It is impossible to predict the exact behavior of the unit cell size and shape with increasing pressure, and thus such reconstructed $g(r)$ ’s cannot be obtained in the absence of a simulation. The fact that the $g(r)$ at 70 kbar can be obtained from the atomic configuration at 10 kbar shows that, at least in our simulations, no solid–solid transition is observed within this pressure range. This is in agreement with the behavior of first-order quantities (Figure 2) with pressure.

3.3. Conformation. The distribution of CCCC torsional angles at various pressures is shown in Figure 10. The presence of gauche population at 1 and 5 kbar signifies the liquid state, whereas the chains adopt an all-trans conformation in the crystal. The pressure-induced changes in the population of gauche conformers of *n*-alkanes across the solid–liquid transition was studied using Raman scattering experiments.^{25,26}

3.4. Dynamics. **3.4.1. Vibrational Density of States.** There are two methods to obtain the classical vibrational density of states: (i) The atomic displacements relative to the equilibrium

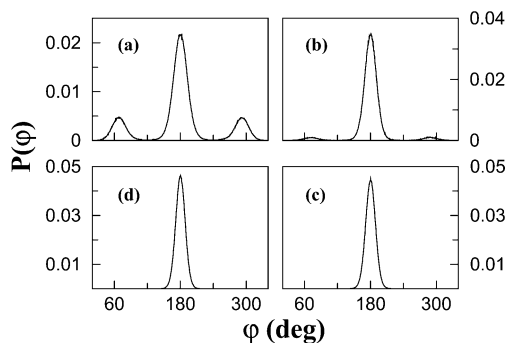


Figure 10. Distribution of the torsional angle, ϕ , around the C–C bond of the alkane backbone shown at different pressures across the solid–liquid transition: (a) 1, (b) 5, (c) 7.5, and (d) 10 kbar.

positions are approximated to be harmonic, and a matrix of the second derivative of the total potential energy of the system with respect to these displacements (i.e., a Hessian) is constructed. The eigenvalue spectrum of this matrix is the vibrational density of states within the harmonic approximation, and the corresponding eigenvectors are related to atomic displacements excited in a mode of that frequency. (ii) The VDOS can also be calculated as the power spectrum (cosine transform) of the velocity autocorrelation function (VACF) of the atoms in the system. Unlike the Hessian method that does not need any dynamical trajectory to be generated, this method needs an MD trajectory. However, it includes anharmonic contributions as well.

We have carried out both of these calculations for *n*-heptane under pressure. The VDOS at 10 kbar obtained from these methods is compared against the dynamic structure factor obtained from a quasielastic-neutron-scattering experiment (Figure 11a–c). Note that the experiment was performed for the crystal at a temperature of 100 K and a pressure of 1 bar, whereas the spectra from simulations are at 300 K and 10 kbar. The agreement between the two computational methods and with the experiment is good. The power spectrum of the VACF has better-resolved peaks than the NMA spectrum at low frequencies (less than 200 cm^{-1}), indicating the significant role of anharmonic effects in these modes.

The features near 3000 cm^{-1} correspond to the C–H stretching modes (not shown). Various peaks in the C–C stretching region (1030–1140 cm^{-1}) and the H–C–H bending region (1300–1500 cm^{-1}) are reproduced well in the simulations because they are built within the model for intramolecular interactions. Of interest to us are the spectral features that correspond to methyl rocking (850–910 cm^{-1}),²⁷ the longitudinal acoustic mode (LAM-3) at 435 cm^{-1} , the methyl torsion mode (250–280 cm^{-1}), and modes in the far-infrared region (<200 cm^{-1}). The modes are assigned on the basis of the visualization of atomic displacements obtained through the normal-mode analysis. The low-frequency assignments are compared to the work of Braden et al.,^{28,29} and the high-frequency modes are compared with the work of Snyder et al.³⁰ Marginal differences are noticed between the peak positions obtained from the normal-mode analysis and that obtained from the VACF. The peaks are much better resolved in the latter, particularly at low frequencies.

3.4.2. Pressure Dependence of VDOS. The VDOS calculated from the VACF at various pressures ranging from 10 to 70 kbar is shown in Figure 12. In general, most vibrational bands shift to higher frequencies with increasing pressure, consistent with infrared spectroscopic measurements.¹⁰ The bands also broaden, possibly because of phonon–phonon interactions and also

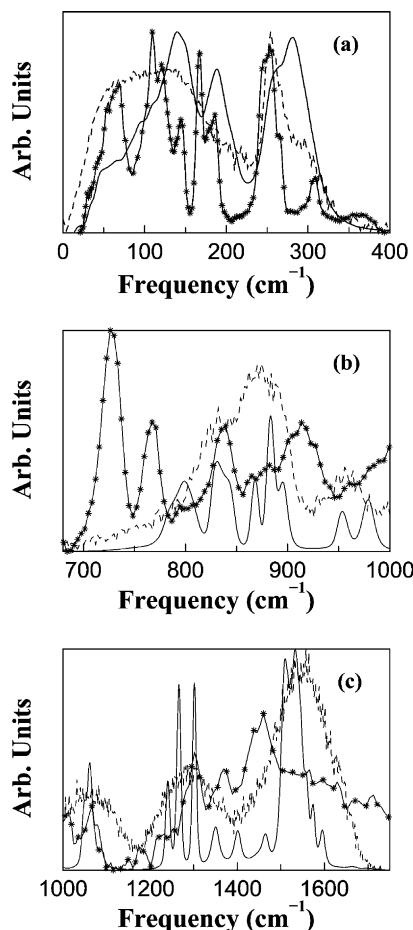


Figure 11. Vibrational density of states obtained from normal-mode analysis (---) and from the velocity autocorrelation function (—*) compared with neutron-scattering data (---*).³⁸ Note that the experimental data is the dynamic structure factor of *n*-heptane at atmospheric pressure and 100 K, whereas the theoretical results are obtained from MD configurations at 10 kbar and 300 K. (a) 0–400, (b) 680–1000, and (c) 1000–1750 cm^{-1} .

because of reduced phonon lifetimes. Significantly, at high pressure some vibrational features are found to disappear from the spectrum or are most likely subsumed under neighboring peaks. The peak at 146 cm^{-1} corresponds to transverse acoustic mode (TAM) vibrations and is found to decrease in intensity at high pressure. TAM vibrations involve atomic displacements in directions perpendicular to the molecular long axis. Hence they will be affected by changes in the intermolecular structure within a crystalline layer. The TAM feature at 260 cm^{-1} that corresponds to methyl rotation (or end-group torsion) is considerably weakened with increasing pressure. We show (later) that although the rotation of the methyl group slows down at 70 kbar it is not completely arrested. The finite intensity of the spectrum at this frequency confirms this fact. Similarly, the peak at around 870 cm^{-1} nearly vanishes at high pressure. This peak corresponds to methyl rocking motions. These observations are consistent with the details of the structure discussed earlier. The symmetric methyl bending modes at 1350 cm^{-1} ^{32,33} also show interesting changes with pressure. The intensity of the peak diminishes rapidly with increasing pressure, and it becomes a plateau at 70 kbar. The C–C stretching region (1030–1140 cm^{-1}) consists of three peaks (at 1048, 1061, and 1080 cm^{-1}) at low pressure, which is consistent with experiments.^{10,30} These modes exhibit a blue shift, whereas the peak at 1048 cm^{-1} vanishes at high pressure. Three peaks corresponding to methyl rocking are present in the range of 850–910 cm^{-1} . They too

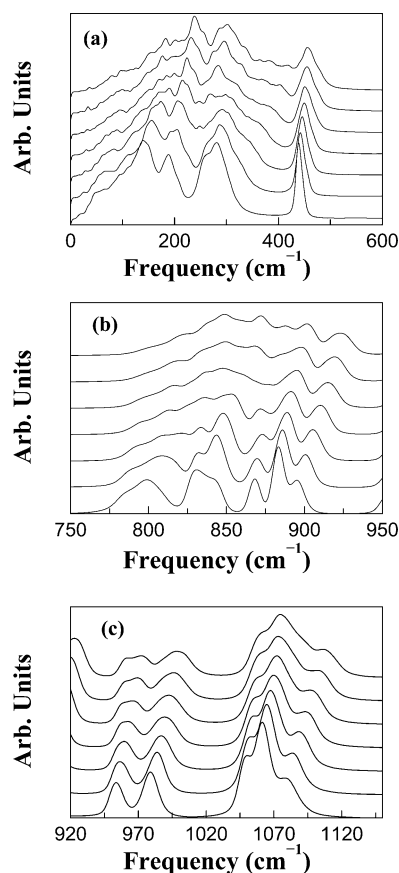


Figure 12. Vibrational density of states obtained by Fourier transformation of the velocity autocorrelation function shown at different pressures in three ranges of frequencies. The functions are shifted for clarity. Pressures (from bottom to top): starting from 10 up to 70 kbar in steps of 10 kbar. (a) 0–600, (b) 750–950, and (c) 920–1150 cm^{-1} .

show a shift to higher frequencies with increasing pressure. Whereas two peaks (884 and 895 cm^{-1}) shift systematically with increasing pressure, the peak at 868 cm^{-1} vanishes at high pressure. The pressure dependence of the methyl rocking mode that we have observed is consistent with the results inferred for *n*-pentane.³¹

Thus, the distribution of the vibrational frequencies generated from the normal-mode analysis captures all of the essential features of the experimental spectra. The additional advantage that one gains from the NMA is the atomic displacements associated with a given vibrational mode. The atomic displacements are related to the eigenvectors obtained from the NMA. We have investigated the nature of atomic motions at selected frequencies and present these results in Figure 13a and b. The procedure that we follow to analyze the atomic displacements is as follows: We select a frequency at which the VDOS exhibits a peak and pick up a few molecules that undergo large-amplitude displacements in modes excited at such frequencies. The modes were assigned on the basis of the visualization of atomic displacements. The vibrational mode at 54 cm^{-1} shown in Figure 13a is a longitudinal mode in which the atomic displacements are along the chain axis of the molecule. The nature of the atomic displacements shown for the mode at 140 cm^{-1} suggests that it is a transverse mode with atomic vibrations perpendicular to the long axis of the molecule. The eigenvectors shown for the mode at 237 cm^{-1} (Figure 13b) can be conveniently assigned to methyl rotation, and that at 817 cm^{-1} can be associated with the methyl rocking mode. The umbrella motion of the methyl group is evident from the modes at 1351

and 1353 cm^{-1} , which is consistent with the experiments of Jona et al.³² and Snyder.³³

3.4.3. Mode Properties. A large amount of information on the modes can be obtained by calculating quantities such as the participation ratio and the phase quotient. The participation ratio (PR_{*j*}) of the *j*th eigenmode is defined as³⁴

$$\text{PR}_j = \frac{\left(\sum_{i=1}^N |\vec{u}_{ij}|^2 \right)^2}{N \sum_{i=1}^N |\vec{u}_{ij}|^4} \quad (2)$$

and the phase quotient (PQ_{*j*}) is defined as

$$\text{PQ}_j = \frac{1}{N_b} \sum_i \sum_k \frac{\vec{u}_{ij} \cdot \vec{u}_{kj}}{|\vec{u}_{ij}| |\vec{u}_{kj}|} \quad (3)$$

where \vec{u}_{ij} is the displacement vector of atom *i* in vibrational mode *j*, *N* is the total number of atoms, and *N_b* is the total number of bonds present in the system. The double summation in eq 3 denotes all bonded pairs of atoms *i* and *k*. The participation ratios at 10 and 70 kbar are plotted in Figure 14a against the frequency of the modes. Large values of PR imply that a significant fraction of the system participates in that particular mode. A value of unity is obtained when all *N* atoms of the system get displaced by the mode. As expected, this value is obtained for the rigid body translational mode at zero frequency. At 10 kbar, the PR value is large at frequencies less than 100 cm^{-1} . Larger values are also observed for the methyl rotation at 250 cm^{-1} . The pressure dependence of PR is interesting. At 70 kbar, the frequency range of large PR values gets extended up to about 300 cm^{-1} . Moreover, the values are also marginally larger (about 0.27) compared to the values at 10 kbar of about 0.25. The PR of the methyl rocking mode at around 880 cm^{-1} and the vibrational modes around 960, 1080, and 1575 cm^{-1} undergo significant changes with increasing pressure. Although the participation ratio of these modes increases with pressure, the prominent changes at 880 cm^{-1} can be attributed to the fact that the environment of the end methyl groups is affected significantly by increasing pressure. The increased PR values are a consequence of increased order in the system. Modes tend to localize because of disorder. In a perfect crystal, all modes will be extended. We have already discussed the increase in structural ordering using pair correlation functions. This result for PR ties in well with the data on the evolution of structure with pressure.

The vibrational modes can be further classified as opticlike and acousticlike on the basis of the phase relationship between the vibrations of the bonded pair of atoms. The phase quotient (PQ) defined in eq 3 is a measure of such a phase relationship, and it is the average cosine of the angle between the displacement vectors of a bonded pair of atoms. PQ can take values between −1 and +1 corresponding to out-of-phase and in-phase vibrations of neighboring (bonded) atoms, respectively. Thus, PQ values are close to +1 for acousticlike modes and are around −1 for opticlike modes.

The data on the phase quotient (PQ) is also quite instructive. This is shown in Figure 14b against frequency at 10 and 70 kbar. A positive value of PQ indicates that the mode has acoustic character, and a negative value implies optic character. All modes of vibration below about 300 cm^{-1} are acoustic in nature, whereas modes in the frequency range of 1000–1200 cm^{-1} are

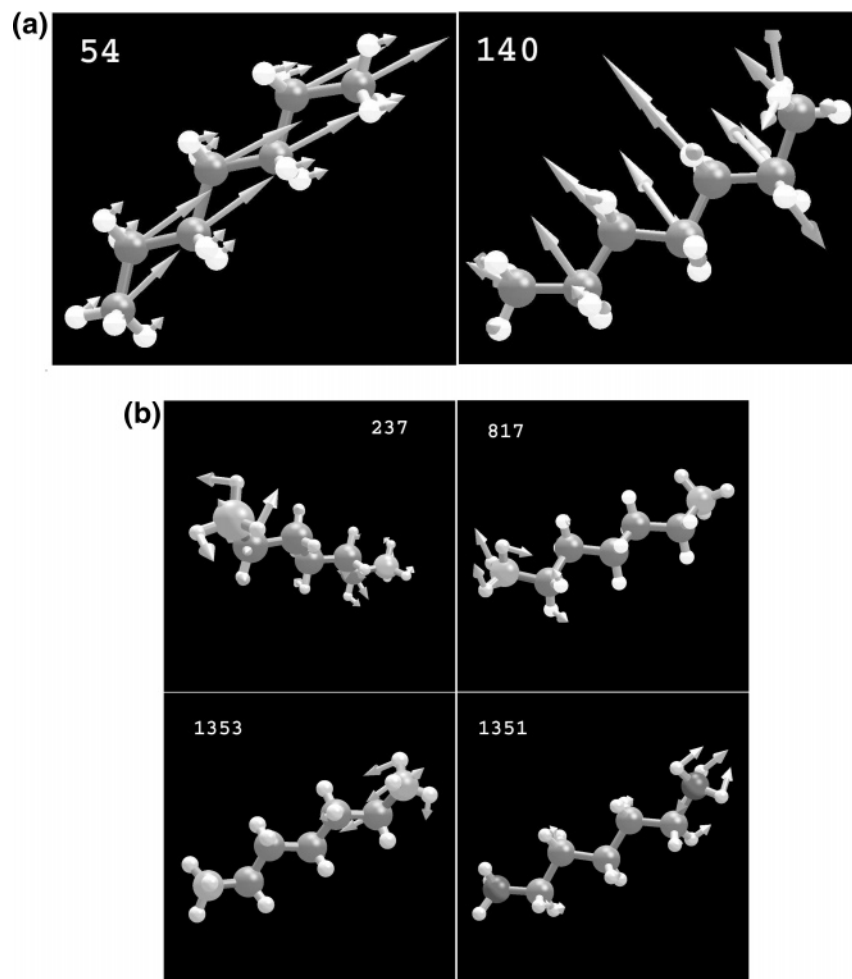


Figure 13. Atomic displacement vectors of a molecule exhibiting large-amplitude motion shown at different frequencies: (a) 54 cm^{-1} (longitudinal vibrations); 140 cm^{-1} , (b) 237 cm^{-1} (methyl rotation); 817 cm^{-1} (methyl rocking); 1351 and 1353 cm^{-1} (umbrella motion of methyl group^{32,33}).

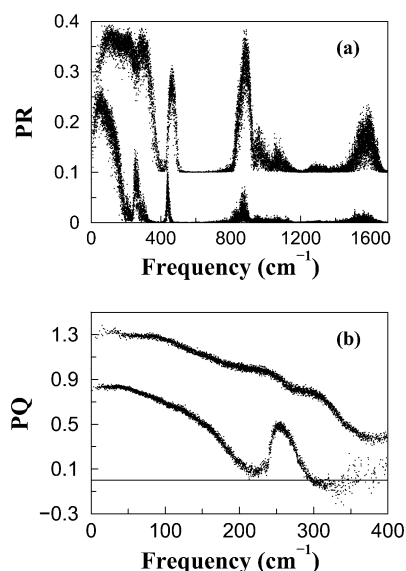


Figure 14. Pressure dependence of the (a) participation ratio and (b) phase quotient of vibrational modes shown against the frequency of the mode at 10 (bottom) and 70 kbar (top). The high-pressure data is shifted up from that at 10 kbar for the sake of clarity.

optic modes. These observations agree well with earlier assignments of LAM and TAM modes at low frequency.^{28,29}

3.4.4. Methyl Rotation. The methyl rotational mode at around 250 cm^{-1} is particularly interesting and is found to occur at the

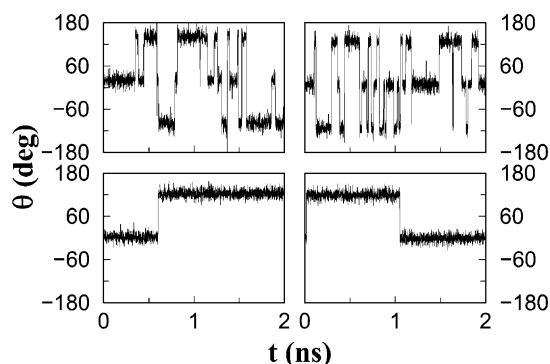


Figure 15. Time evolution of the angle, θ , between a CH vector of a methyl group at time t and at time zero shown for two molecules chosen arbitrarily. Left panels: molecule 1; right panels: molecule 2. Top: at 10 kbar; bottom: at 70 kbar.

same frequency in all linear alkanes.²⁸ To illustrate the nature of this rotation, we show in Figure 15 the time dependence of the angle subtended by a CH vector of a methyl group of a molecule at time t with the same vector at time zero. These are plotted at 10 and 70 kbar for two arbitrary molecules. Note the rather sharp nature of the transitions from one orientation of the CH vector to another, which are separated by 120°. These processes are single-molecule events of methyl rotation. Not so surprisingly, one observes many fewer transitions at 70 kbar relative to the data at 10 kbar. We now examine this mode further by studying the time correlation function (TCF) of the CH vector of the methyl group.

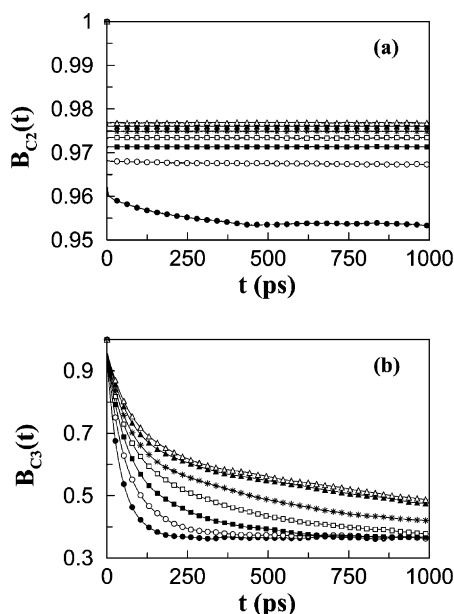


Figure 16. Rotational time correlation functions of an HCH bisector that belongs to (a) a methylene group, $B_{c2}(t)$, and (b) a methyl group, $B_{c3}(t)$, shown at different pressures. Pressures (from bottom to top): starting from 10 up to 70 kbar in steps of 10 kbar. The initial decay of the function in graph a is faster than 1 ps. Symbols are shown infrequently for clarity.

One can obtain an estimate of the time scales of the rotation of the methyl groups by calculating a normalized time correlation function (TCF) defined as

$$B(t) = \frac{\langle \vec{R}(0) \cdot \vec{R}(t) \rangle}{\langle \vec{R}(0) \cdot \vec{R}(0) \rangle} \quad (4)$$

where $\vec{R}(t)$ is the HCH bisector vector at time t . In what follows, $B_{c2}(t)$ denotes the TCF of the HCH bisector vector of methylene groups, and $B_{c3}(t)$ represents that of the HCH bisector belonging to CH_3 groups.

Figure 16a and b shows the behavior of both $B_{c2}(t)$ and $B_{c3}(t)$ at various pressures. Two important features are to be noted: (a) At all pressures, $B_{c3}(t)$ decays to lower values, but $B_{c2}(t)$ does not decay at all. (b) The rate of decay of $B_{c3}(t)$ decreases with increasing pressure, but $B_{c2}(t)$ does not show much change with pressure. It is clear from these observations that the HCH bisector belonging to the CH_3 group is able to explore different orientations at low pressures than the HCH bisector of the CH_2 group. This points to the additional free volume available to the methyl end-groups, whereas the packing around CH_2 is rigid. In addition, the slowing down of the decay of $B_{c3}(t)$ at higher pressures suggests that the environment of a methyl group is altered at higher pressures than for a methylene group. This can be attributed to the reduction of available volume for the CH_3 groups with increasing pressure. Note that the HCH bisector of CH_3 can explore only half of the sphere around the methyl carbon and the remaining half is forbidden because of the presence of the chain backbone. This explains the nonzero saturation value of $B_{c3}(t)$ at long time. Although the above analysis provides an idea of the methyl group rotation, it does not resolve the issue of whether the rotation is a full rotation about the terminal C2–C3 bond. To address this, we have divided $B_{c3}(t)$ into two parts: $B_{c3}^\perp(t)$ evaluates the TCF of the HCH bisector of the methyl group projected onto a plane perpendicular to the terminal C2–C3 bond, and $B_{c3}^\parallel(t)$ determines the TCF of the HCH bisector of CH_3 along the terminal

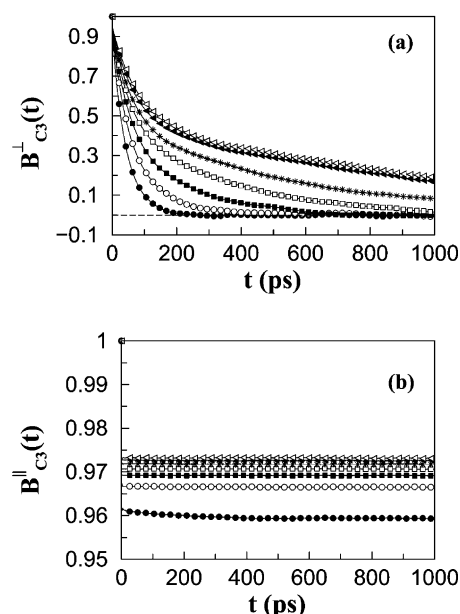


Figure 17. Rotational time correlation functions of an HCH bisector for atoms belonging to a methyl group (a) projected onto a plane perpendicular to the terminal C2–C3 bond of the n -heptane chain, $B_{c3}^\perp(t)$ and (b) projected along (i.e., parallel to) the terminal C2–C3 bond, $B_{c3}^\parallel(t)$, shown at different pressures. Pressures (from bottom to top): starting from 10 up to 70 kbar in steps of 10 kbar. The initial decay of the function in graph (b) is faster than 1 ps. Symbols are shown infrequently for clarity.

TABLE 2: Biexponential Fit of the Form $B_{c3}^\perp(t) = w_1 e^{-t/\tau_1} + (1 - w_1) e^{-t/\tau_2}$ to the Data Presented in Figure 17

P (kbar)	τ_1 (ps)	w_1 (%)	τ_2 (ps)	$\langle \tau \rangle$ (ps)
10	44.4	90	0.6	40.2
20	96.0	63	24.7	69.7
30	180.0	54	34.6	112.6
40	297.7	55	36.9	179.7
50	567.7	47	51.9	294.9
60	1000.0	48	59.0	509.6
70	954.3	52	60.2	527.4

C2–C3 bond. In Figure 17a and b, we show the behavior of $B_{c3}^\perp(t)$ and $B_{c3}^\parallel(t)$. At low pressures, $B_{c3}^\perp(t)$ decays to zero within the time scales of the analysis, and at higher pressures, the TCF slows down considerably. The decay to a value of zero indicates the full rotation of the methyl group about the C2–C3 axis. Expectedly, the TCF for the function parallel to the C2–C3 bond ($B_{c3}^\parallel(t)$) does not decay at all.

We have fit $B_{c3}^\perp(t)$ to a multiexponential function and have obtained time constants for methyl rotation. The data could not be fit to a single exponential, and hence a two-exponential function was used. The parameters of the fit along with the average time constants are provided in Table 2. At 10 kbar, the behavior is nearly single-exponential with a time constant of around 40 ps. This increases precipitously to nearly 1 ns at 70 kbar. Beyond 10 kbar, an additional contribution emerges in the decay of $B_{c3}^\perp(t)$, whose time constant is surprisingly small, on the order of tens of picoseconds. Currently, we are not clear about the origin of these two time scales. This needs to be probed further.

The increase in pressure decreases the free volume available for rotation for the methyl group and increases the energy barrier. As a first step to estimate the barrier for this hindered rotation, we have calculated the probability of the projection of a methyl CH vector onto the plane perpendicular to the terminal C2–C3 vector to be oriented at an angle θ with respect

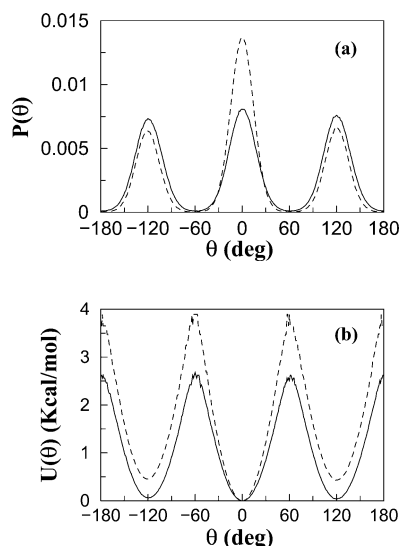


Figure 18. (a) Distribution of the angle, θ , between a CH vector of a methyl group at time t and at time zero shown at 10 kbar (—) and at 70 kbar (---). (b) Potential of mean force (PMF) obtained from the above distribution shown at 10 (—) and at 70 kbar (---).

to its value at $t = 0$. The quantity is defined as

$$P(\theta) = \langle \delta(\theta - \theta_i(t)) \rangle \quad (5)$$

where $\theta_i(t)$ represents the θ of the i th CH vector at time t . The angular brackets imply that the probability distribution is evaluated over CH vectors of all of the methyl groups in the system and over all time. The $P(\theta)$ function shown in Figure 18a exhibits three peaks, one at 0° and others at $\pm 120^\circ$. These peaks signify the three possible states of the CH vector. The time variation of occupation of these states for a single methyl group has been shown in Figure 15. The time scales of the transition between these states has been shown in Figures 16 and 17. Here we study the energy barriers of the transition between these states. At 10 kbar, the intensities of these peaks are equal, implying that it is equally likely that the CH vector is able to explore these states. Upon increasing the pressure, we find the behavior of the $P(\theta)$ function to change significantly. At 70 kbar, the probability of finding the CH vector in the $\theta = 0^\circ$ state is higher than that for the other states within the time scales of simulation. The states at $\theta = \pm 120^\circ$ have an equal likelihood of being visited by the CH vectors. The taller peak at $\theta = 0^\circ$ can be attributed to the restricted dynamics of the CH vectors at higher pressure. These observations are consistent with both the time dependence of θ of tagged molecules shown in Figure 15 and with the TCF of the HCH vector shown in Figure 17b.

On the basis of the knowledge of $P(\theta)$, one can estimate the energy required for a CH vector to transition from the $\theta = 0^\circ$ state to either of the $\theta = \pm 120^\circ$ states. This is done by inverting the probability distribution and obtaining the potential of mean force (PMF), $U(\theta)$, which is a measure of the energy barrier for the hindered methyl rotation, as

$$U(\theta) = -T \ln(P(\theta)) \quad (6)$$

The PMF is shown in Figure 18b at the two extreme pressure conditions. We have shifted the data in such a way that the energy at the $\theta = 0^\circ$ state is 0 kcal/mol. The energy barrier to cross from the initial orientation to the final is obtained as the energy difference between the state at angles 120 and 0° . The barrier height is calculated to be 2.6 and 3.8 kcal/mol at 10 and

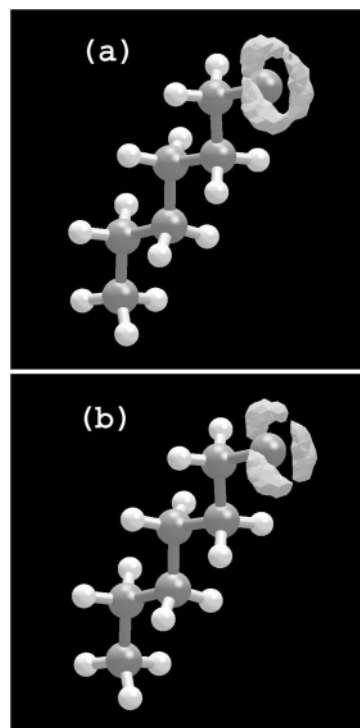


Figure 19. Atomic probability density map of methyl hydrogen around the carbon atom shown at (a) 10 and (b) 70 kbar. The probability density values greater than 0.0002 hydrogen atoms/ \AA^3 are shown for clarity.

70 kbar, respectively, and their magnitudes compare well with experiments.^{35–37} A caveat needs to be added here regarding this analysis. Evidently, at 70 kbar the probability function $P(\theta)$ has not converged to the equilibrium value. At equilibrium, all three states are equally likely. The difference in the heights of the three peaks in Figure 18a at 70 kbar is a consequence of the transition time scale being larger than the time scale of observation. Thus, an inversion of these data to obtain the PMF at 70 kbar is erroneous. However, this educational exercise provides us with an estimate of the barrier height involved in methyl rotation, at least at 10 kbar.

The features observed from the above analyses can be validated by determining the atomic density distribution of hydrogens around the carbon atom of the methyl group. We have carried out such an analysis to show that the methyl group is able to rotate in the solid state at low pressures. To achieve this goal, we need to fix the molecular orientation. We rotate the plane formed by the terminal C3–C2–C2 triplet in such a way that it lies parallel to the xz plane with the z axis coinciding with the C3–C2 bond vector. The density distribution of hydrogen atoms around a C3 atom in this frame was averaged over all molecules and configurations. The results obtained from this analysis are shown in Figure 19 for various pressures. At low pressure, we find that the hydrogen atoms are distributed uniformly to form a circular ring in a plane perpendicular to the C3–C2 bond vector. This scenario changes as a function of increasing pressure, where one finds three lobes in the atomic density map. The presence of distinct regions at high pressure signifies the localization of hydrogen atoms in three specific locations around the C3–C2 bond vector.

4. Conclusions

We have presented extensive atomistic molecular dynamics simulations of crystalline *n*-heptane under pressure conditions that include the liquid–crystal transition as well. The total length

of all MD trajectories is around 23 ns. Such long trajectories have been employed to map precisely the structural and gradual dynamical changes that are wrought by pressure.

We observe signatures of the liquid–solid transition in the structure of the system. Conformational changes, principally the formation of gauche defects, have been studied in the liquid state at pressures below 10 kbar. Above 10 kbar, with increasing pressure, significant changes occur in the environment around the methyl group rather than around the methylene groups. Pair correlation and angle distribution functions reveal that at 10 kbar the first coordination shell of CH₃ contains around 10 neighbors that are loosely packed. At 70 kbar, this neighbor shell resolves into specific subshells that contains four CH₃ neighbors from the layer across the central CH₃ and six neighbors that belong to the same layer. Within the latter, two CH₃ groups are present that are farther than the other four methyls. Angle distributions and probability density maps for CH₃ groups within the first coordination shell have shown their precise locations. These subtle changes in the crystalline phase, however, are not accompanied by any discontinuities in first-order thermodynamic quantities, such as the volume, cell parameters, or the internal energy of the system. On the basis of these calculations, we are thus led to believe that the increase in pressure does not lead to a first-order solid–solid transition. A preliminary examination of the isothermal compressibility does not show any discontinuity with increasing pressure, thus also diminishing the possibility of a second-order transition.

However, various issues such as system size effects, time scales associated with the transition, and the accuracy of the interaction potentials, particularly at high densities, need to be considered before one can safely rule out any solid–solid transition. Despite the long runs adopted here, the system may have been evolving along a metastable path because of long relaxation times at high densities. This could preclude the experimentally alluded to transition at 30 kbar in the simulations and needs to be investigated further. Although the empirical nature of the interaction potential could shift the solid–solid transition toward higher pressures, the success of the present interaction model in characterizing the phase behavior of *n*-alkanes¹⁴ guides us to believe that the highest pressure employed here is large enough for the transition to occur.

We have also studied the vibrational dynamics of this system. The vibrational density of states has been computed within the harmonic approximation through normal-mode analysis as well as through the velocity autocorrelation function method. Results obtained from these two methods agree with each other and with inelastic-neutron-scattering experiments³⁸ and spectroscopic data.^{10,30,33} We find a blue shift in nearly all of the vibrational bands as a function of pressure. In particular, the low-frequency modes shift by as much as 45 cm^{−1}. The width of the bands increases with pressure, in agreement with infrared experiments. Some of the bands, such as the TAM vibration at 146 cm^{−1} and the methyl rocking mode at 800 cm^{−1}, nearly vanish at 70 kbar. The normal-mode analysis enabled us to visualize the modes to aid in their assignments. The methyl rotational mode at 260 cm^{−1} was also investigated through a time correlation function of the projection of the CH vector on the plane perpendicular to the C2–C3 axis. We found the methyl groups to rotate even at high pressures, although considerably slower than at 10 kbar.

The comprehensive characterization of this system in terms of thermodynamics, structure, vibrational analysis, and dynamics leads us to conclude that there is no first-order solid–solid transition in the *n*-heptane model under pressure up to 70 kbar.

Acknowledgment. We acknowledge the Centre for Development of Advanced Computing, Bangalore, India, for a generous time allocation in their Central Terascale Supercomputing Facility, where these calculations were performed. We thank Professor Preston Moore and Mr. Sagar Sen for the molecular visualization program used in the production of some figures in this paper. M.K. acknowledges CSIR, India for a senior research fellowship.

References and Notes

- (1) Small, D. M. *The Physical Chemistry of Lipids*; Plenum Publishing: New York, 1988.
- (2) Chapman, D.; Jones, M.; Jones, M. N. *Micelles, Monolayers and Biomembranes*; John Wiley: New York, 1994.
- (3) Hyun, B.-R.; Dzyuba, S. V.; Bartsch, R. A.; Quitevis, E. L. *J. Phys. Chem. B* **2002**, *106*, 7579.
- (4) Dagaut, P.; Reuillon, M.; Cathonnet, M. *Combust. Sci. Technol.* **1994**, *95*, 233.
- (5) Sirota, E. B.; King, H. E., Jr.; Hughes, G. J.; Wan, W. K. *Phys. Rev. Lett.* **1991**, *68*, 492.
- (6) Ryckaert, J.-P.; Klein, M. L.; McDonald, I. R. *Phys. Rev. Lett.* **1987**, *58*, 698. Ryckaert, J.-P.; Klein, M. L.; McDonald, I. R. *Mol. Phys.* **1994**, *83*, 439.
- (7) Yamamoto, H.; Nemoto, N.; Tashiro, K. *J. Phys. Chem. B* **2004**, *108*, 5827.
- (8) Guillaume, F.; Ryckaert, J.-P.; Rodriguez, V.; MacDowell, L. G.; Girard, P.; Dianoux, A. J. *Phase Transitions* **2003**, *76*, 823.
- (9) Boese, R.; Weiss, H. C.; Bläser, D. *Angew. Chem., Int. Ed.* **1999**, *38*, 988.
- (10) Yamaguchi, M.; Serafin, S. V.; Morton, T. H.; Chronister, E. L. *J. Phys. Chem. B* **2003**, *107*, 2815.
- (11) Merle, A. M.; Lamotte, M.; Risemberg, S.; Hauw, C.; Gaultier, J.; Grivet, H. Ph. *Chem. Phys.* **1977**, *22*, 207.
- (12) Chen, B.; Martin, M. G.; Siepmann, J. I. *J. Phys. Chem. B* **1998**, *102*, 2578. Chen, B.; Siepmann, J. I. *J. Phys. Chem. B* **1999**, *103*, 5370.
- (13) Tobias, D. J.; Tu, K.; Klein, M. L. *J. Chim. Phys. Phys.-Chim. Biol.* **1997**, *94*, 1482.
- (14) Polson, J. M.; Frenkel, D. *J. Chem. Phys.* **1999**, *111*, 1501.
- (15) Krishnan, M.; Balasubramanian, S.; Clarke, S. *J. Chem. Phys.* **2003**, *118*, 5082.
- (16) Parrinello, M.; Rahman, A. *Phys. Rev. Lett.* **1980**, *45*, 1196.
- (17) Martyna, G. J.; Tuckerman, M. E.; Tobias, D. J.; Klein, M. L. *Mol. Phys.* **1996**, *87*, 1117.
- (18) Martyna, G. J.; Klein, M. L.; Tuckerman, M. *J. Chem. Phys.* **1992**, *97*, 2635.
- (19) Tuckerman, M. E.; Berne, B. J.; Martyna, G. J. *J. Chem. Phys.* **1992**, *97*, 1990.
- (20) Allen, M. P.; Tildesley, D. J. *Computer Simulation of Liquids*; Clarendon: Oxford, 1987.
- (21) Tuckerman, M. E.; Yarne, D. A.; Samuelson, S. O.; Hughs, A. L.; Martyna, G. J. *Comput. Phys. Commun.* **2000**, *128*, 333.
- (22) Krishnan, M.; Balasubramanian, S. *Phys. Rev. B* **2003**, *68*, 064304.
- (23) Paci, E. *Biochim. Biophys. Acta* **2002**, *1595*, 185.
- (24) Bagchi, K.; Balasubramanian, S.; Klein, M. L. *J. Chem. Phys.* **1997**, *107*, 8561.
- (25) Schoen, P. E.; Priest, R. G.; Sheridan, J. P.; Schnur, J. M. *J. Chem. Phys.* **1979**, *71*, 317.
- (26) Snyder, R. G. *J. Chem. Phys.* **1982**, *76*, 3921.
- (27) Gorce, J. P.; Spells, S. J.; Zeng, X. B.; Ungar, G. *J. Phys. Chem. B* **2004**, *108*, 3130.
- (28) Braden, D. A.; Parker, S. F.; Tomkinson, J.; Hudson, B. S. *J. Chem. Phys.* **1999**, *111*, 429.
- (29) Tomkinson, J.; Parker, S. F.; Braden, D. A.; Hudson, B. S. *Phys. Chem. Chem. Phys.* **2002**, *4*, 716.
- (30) Snyder, R. G.; Schachtschneider, J. H. *Spectrochim. Acta* **1963**, *19*, 85.
- (31) Kato, M.; Taniguchi, Y. *J. Chem. Phys.* **1991**, *94*, 4440.
- (32) Jona, P.; Gussoni, M.; Zerbi, G. *J. Mol. Struct.: THEOCHEM* **1985**, *119*, 329.
- (33) Snyder, R. G. *J. Mol. Spectrosc.* **1961**, *7*, 116.
- (34) Taraskin, S. N.; Elliott, S. R. *Phys. Rev. B* **1997**, *56*, 8605.
- (35) Morelon, N. D.; Kneller, G. R.; Ferrand, M.; Grand, A.; Bee, M. *J. Chem. Phys.* **1998**, *109*, 2883.
- (36) Chatfield, D. C.; Augsten, A.; D'cunha, C.; Wong, S. E. *J. Comput. Chem.* **2003**, *24*, 1052.
- (37) Kundu, T.; Pradhan, B.; Singh, B. P. *Proc. — Indian Acad. Sci., Chem. Sci.* **2002**, *114*, 623.
- (38) <http://www.isis.rl.ac.uk/insdatabase/ascii/Heptane.dat>